

Airborne Water Vapor DIAL and in situ Observations of a Sea-Land Interface

by G. EHRET¹, A. GIEZ¹, C. KIEMLE¹, K. J. DAVIS², D. H. LENSCHOW², S. P. ONCLEY²
and R. D. KELLY³

¹Institute of Atmospheric Physics, DLR, Oberpfaffenhofen, Germany

²National Center for Atmospheric Research, P.O. Box 3000, Boulder, CO 80307-3000, USA

³University of Wyoming, Laramie, Wyoming, USA

(Manuscript received February 3, 1995; accepted September 14, 1995)

Abstract

Two contrasting boundary layers in an enclosed valley are observed with a water vapor differential absorption lidar (DIAL) and in situ instruments on board the National Center for Atmospheric Research (NCAR) Electra and University of Wyoming King Air research aircraft. Lidar observations of water vapor and aerosols agree very well with in situ observations over agricultural land in the Imperial Valley of California and the Salton Sea. DIAL water vapor profiles averaged over 12 km in the horizontal and 200 m in the vertical are within 10 % of in situ measurements. Lidar observations reveal the very heterogeneous nature of the planetary boundary layer (PBL) over land, and show a pronounced difference in PBL structure between the land and sea. The structure superficially resembles a sea breeze, but in situ observations reveal an advected convective boundary layer mixing into a stably-stratified layer that overlies a much shallower PBL over the sea. The observations show the benefit of complementary remote profiling and in situ observations in airborne studies of the planetary boundary layer (PBL). The airborne DIAL system is proven capable of describing very fine boundary-layer structure in aerosol backscatter, and water vapor features on the scale of about 200 m in the vertical and a few kilometers in the horizontal.

Zusammenfassung

Flugzeuggetragene Wasserdampf-DIAL und In Situ Beobachtungen eines See-Land Übergangs

Mit einem Wasserdampf Differential-Absorptions Lidar (DIAL) und In Situ Instrumenten an Bord der Forschungsflugzeuge Electra des National Center for Atmospheric Research (NCAR) und der King Air der Universität Wyoming wurden zwei unterschiedliche Grenzschichtsituationen in einem abgeschlossenen Tal untersucht. Die Lidar-Beobachtung von Wasserdampf und Aerosolen stimmen sehr gut mit den In Situ Beobachtungen über landwirtschaftlich genutztem Land im kalifornischen Imperial Valley und über der Salton Sea überein. Die DIAL-Wasserdampfprofile stimmen bei einer Mittelung von horizontal 12 km und vertikal 200 m innerhalb von 10 % mit den In Situ Messungen überein. Die Lidarbeobachtungen zeigen die sehr heterogene Natur der planetarischen Grenzschicht (PBL) über Land und den deutlichen Unterschied in der PBL-Struktur zwischen Land und See. Oberflächlich betrachtet ähnelt die Struktur am Übergang von Land und See einer Seebrise, jedoch deuten die In Situ Beobachtungen auf eine seitlich eingeströmte konvektive Grenzschicht hin, welche sich mit der stabilen, stratiformen Luft mischt, die über der deutlich weniger ausgeprägten Grenzschicht der See liegt. Die Beobachtungen zeigen den Vorteil der Kombination der zwei Meßmethoden Fernerkundung und In Situ-Messung bei der Untersuchung der planetaren Grenzschicht mit dem Flugzeug. Das flugzeuggetragene DIAL-System hat gezeigt, daß damit sehr kleinskalige Strukturen in der Grenzschicht erkannt werden und Wasserdampfverteilungen auf einer Skala von etwa 200 m vertikal und einigen km horizontal aufgelöst werden können.

1 Introduction

Aircraft have become widely used as platforms for investigating the structure of the planetary boundary layer (PBL) and turbulent transport within the PBL. When presented with significant vertical and horizontal heterogeneity, however, in situ observations can be difficult to interpret. In these situations, airborne remote sensing in combination with in situ observations provides a much more detailed picture of the PBL. Airborne remote profiling techniques are also capable of describing large portions of the atmosphere much more quickly than can be done with in situ airborne instruments, though typically at the expense of some degree of instrumental accuracy.

Water vapor and aerosols both exhibit very heterogeneous distributions in the PBL. The distribution of water vapor in the PBL is a critical factor in boundary layer cloud development, atmospheric dynamics, and interactions between the atmosphere and the earth's surface. Aerosols serve as excellent air mass tracers and have important effects on the earth's radiation budget. High spatial and temporal resolution observations of these quantities with sufficient accuracy to resolve PBL structures would be very beneficial to airborne studies.

By detecting the backscatter of a short laser pulse emitted into the atmosphere, a lidar (LIght Detection And Ranging) is capable of measuring the range resolved distribution of aerosols and thin clouds. A Differential Absorption Lidar (DIAL) uses laser pulses of two different wavelengths, with one centered on an absorption line of a trace gas. The comparison of the backscatter at this wavelength with the signal at the nearby non-absorbed wavelength yields the trace gas concentration as a function of distance from the lidar. When the lidar is operated on an aircraft it can measure two dimensional cross-sections of aerosol backscatter and water vapor concentration along the flight track.

An airborne water vapor DIAL has been developed by the German Aerospace Research Establishment (DLR) at Oberpfaffenhofen, Germany. First measurements performed in the lower troposphere demonstrated the system's ability to measure two-dimensional aerosol and water vapor distributions during daytime conditions (Ehret et al., 1990). The system has since been deployed in an operational mode during the EFEDA '91 (European Field Experiment in a Desertification Threatened Area) field experiment, measuring the aerosol and water

vapor boundary layer structure over a semiarid area in central Spain which is threatened by the possibility of gradual desertification (Kiemle et al., 1995), and during the German CLEOPATRA (Cloud Experiment in Oberpfaffenhofen und Transport) field campaign, where precipitable water obtained from DIAL measurements was compared with the measurements from a multifrequency passive microwave radiometer system (Meischner et al., 1994). For these experiments the DIAL looked downward from the DLR Falcon20 research aircraft.

In 1994 the system was used in the BOREal Ecosystem-Atmosphere Study (BOREAS) onboard the National Center for Atmospheric Research (NCAR) Electra research aircraft to investigate the structure, height and variability of the PBL over the boreal forest as well as the water vapor distribution in and above the PBL. Because of the vibrational noise level of the turboprop aircraft, the restriction of having a lidar port on the side of the fuselage only, and the need to measure large humidities over a short range, major modifications of the DIAL hardware and software were necessary. A pre-BOREAS test campaign took place in the Imperial Valley of California in December of 1993 to test the performance of the modified system on the new platform.

Two aircraft took part in this campaign, the NCAR Electra and the University of Wyoming King Air. Both carried an extensive array of in situ instruments designed for high frequency measurements of air velocity, scalars and radiation in addition to the DLR DIAL on board the Electra. This paper reports measurements taken during that campaign. We demonstrate the accuracy of the DIAL system, and the complementary nature of airborne in situ and DIAL observations for describing boundary layer structure.

2 Instrumentation

2.1 The Water Vapor DIAL System

2.1.1 The Differential Absorption Principle

The differential-absorption technique can be used to measure water vapor profiles using near infrared lidar (Schotland, 1966). Measurements are typically performed at two wavelengths, one at the line center (on-line) and one on the wing (off-line) of an appropriate water vapor absorption line. The mean water vapor molecular number density, $N(R)$, for

range cell $\Delta R = R_2 - R_1$ at distance $R = R_1 + \Delta R/2$ can be calculated with the well known DIAL equation approximation (Schotland, 1974):

$$\bar{N}(R) = \frac{1}{2 \cdot \sigma \Delta R} \cdot \ln \left(\frac{P_{off}(R_2) \cdot P_{on}(R_1)}{P_{on}(R_2) \cdot P_{off}(R_1)} \right). \quad (1)$$

In this equation, P_{on} and P_{off} correspond to the power received from the on-line and off-line wavelengths at distances R_1 and R_2 , respectively. The off-line power is a function of aerosol backscattering and extinction. $\sigma = \sigma_{on} - \sigma_{off}$ is the molecular differential absorption cross section of the selected water vapor line, determined via a Voigt profile calculation using known line parameters from Grossmann and Browell (1989a,b). When temperature insensitive lines are selected, as during pre-BOREAS, this calculation can be performed with temperature and pressure profiles known from climatological studies (Browell et al., 1991). In the case of a DIAL laser with high spectral purity and a line width that is much smaller than the water vapor line width, the absorption cross section is given by $\sigma(\nu_0)$ where ν_0 denotes the wavenumber of the absorption line center.

In our case the spectral purity of the laser is not sufficient and the determination of σ is more complex. A careful analysis of the spectral profile of the DIAL laser has shown that the narrow-band laser line is accompanied by additional background emission (Ehret et al., 1993). Thus the laser line profile cannot be treated as an ideal monochromatic profile, and the spectral behavior has to be accounted for in Eq. (1). This is realized by introducing an effective differential absorption cross section

$$\sigma_{eff} = \frac{\int_0^{\infty} \sigma(\nu) [L(\nu - \nu_{on}) - L(\nu - \nu_{off})] d\nu}{\int_0^{\infty} L(\nu) d\nu}, \quad (2)$$

where ν is the wavenumber in cm^{-1} , $L(\nu)$ is a normalized function which describes the spectral profile of the laser, ν_{on} and ν_{off} indicate the wavenumber of the line center and wing measurements, and $\sigma(\nu)$ represents the Voigt profile.

The introduction of σ_{eff} , however, leads to another error source in the DIAL retrieval. It arises from the fact that the on-line laser spectrum is changed by the water vapor absorption (Ismail and Browell, 1989). The narrow-band part of the on-line laser spectrum, which lies in the absorption line center, is

much more strongly attenuated than the background radiation in the line wings. This causes a deformation of the laser line spectral profile $L(\nu - \nu_{on})$ as a function of distance along the laser beam path.

This effect leads to a systematic underestimate of the water vapor concentration if one uses the unmodified laser line profile in Eq. (2) to calculate σ_{eff} . The error depends on the two-way optical depth of the probed atmosphere which itself is a function of the selected line strength and the water vapor number density. At optical depths < 0.3 , typical only of limited ranges or very dry regions in the upper troposphere, the modification of the spectral profile is negligible (Ehret et al., 1993). For measurements in the PBL at optical depths > 0.3 the effective absorption cross section, σ_{eff} , has to be recalculated using the deformed laser line profile. To account for this range dependent effect, we apply an iterative correction procedure. For these calculations, the laser line profile is modeled by a narrow-band laser peak which is absorbed, and a non-absorbed broad-band radiation. The bandwidth of the narrow-band part is measured with a spectrometer which is part of the airborne system. The contribution of the broad-band laser radiation can be uniquely determined from a line intercomparison where the vertical water vapor profiles measured with different strong absorption lines over the same atmospheric region are compared. There is only one, unique laser line spectral profile for which the two water vapor profiles will match.

2.1.2 The DIAL System

The DLR DIAL uses a narrow-band tunable dye laser that sequentially generates the on-line and off-line wavelengths. It is pumped by a frequency-doubled Nd:YAG laser. The Nd:YAG laser operates in a Q-switched mode, to provide short pulses with a repetition rate of 10 Hz. The dye solution Pyridine 1 in methanol contained in a flow cell enables sufficient laser output from the tunable laser system in the near-infrared at 720 nm. In this wavelength region several water vapor lines exist that are suitable for water vapor DIAL measurements in the PBL. On board the aircraft the wavelength of the narrow-band dye laser can be precisely adjusted to the line center of a selected water vapor line using the absorption spectra of a photo-acoustic cell at low water vapor pressure. The laser bandwidth and its wavelength stability are controlled by a Fizeau spectrometer and recorded by the data acquisition system for each shot-pair.

Table 1

DIAL System Parameters	
Laser System	
Laser type:	Nd:YAG pumped dye-laser
Pulse width:	6 nsec
Pulse energy:	typ. 10–15 mJ, max. 30 mJ
Bandwidth:	$\leq 0.03 \text{ cm}^{-1}$ (FWHM)
Spectral purity:	typ. 70–75 %
Repetition rate:	10 Hz
on-/off-line frequency:	4.5 Hz
Wavelength Control	
Wavelength calibration (on-line):	Water vapor filled PAS-cell
Precision:	0.01 cm^{-1}
Bandwidth control:	Fizeau type spectrometer
Spectral resolution:	0.007 cm^{-1}
Resolution of readout:	$0.002 \text{ cm}^{-1}/\text{pixel}$
Receiver System	
Telescope:	35 cm Cassegrain
Spectral filter:	$\Delta\lambda = 0.65 \text{ nm}$, 50 % transmission
Detector:	Photomultiplier Hamamatsu R928
Electronic bandwidth of amplifier:	6 MHz
Digitizer:	12 bit 20 MHz
Data acquisition system:	PDP 11, Q-Bus, CAMAC
Storage medium:	Removable disk 88 Mbyte

The airborne system's receiver consists of a 35 cm diameter Cassegrain telescope which collects the photons backscattered from the atmosphere. The photons passing the receiver optics are detected with a photomultiplier. A three-cavity interference filter is placed in the receiver channel to filter out the unwanted daytime background radiation. The resulting signal is then digitized with a resolution of 12 bits at a sampling rate of 20 MHz for each laser shot. The off- and on-line lidar signals are transmitted at a frequency of approximately 4.5 s^{-1} , and the backscattered signals are sampled from a selected vertical range. A real-time microcomputer which controls the data acquisition system stores these data on a removable cartridge disk for further data processing on the ground. The airborne DIAL system is currently improved. The most important system parameters of the present system are summarized in Table 1.

2.2 In situ Instrumentation

The Electra and King Air use similar instrumentation for both thermodynamic and dynamic measurements. Temperature is measured with Rosemount resistance-wire thermometers, mean water vapor

with chilled mirror dew-point hygrometers, and winds with differential pressure measurements from pressure ports on noseboom radomes combined with inertial navigation system (INS) measurements of airplane velocity and attitude angles. Position was measured both via INS and the Global Position System (GPS). Electra aerosol measurements from 0.1 to $3.1 \mu\text{m}$ diameter were obtained from the Particle Measurements Systems PCASP. Electra radiation surface temperature was obtained from the Barnes PRT-5 infrared radiometer. Lenschow (1986) describes many of the instruments and measurement techniques.

3 Observations

On December 16 and 17, 1993; the NCAR Electra and the University of Wyoming King Air flew coordinated patterns over the Imperial Valley, illustrated in Figure 1. One flight leg, running north-south over 45 km, covered a heavily irrigated patchwork of agricultural fields. The northwest to southeast leg, about 30 km long, crossed the boundary of the agricultural valley and the Salton Sea.

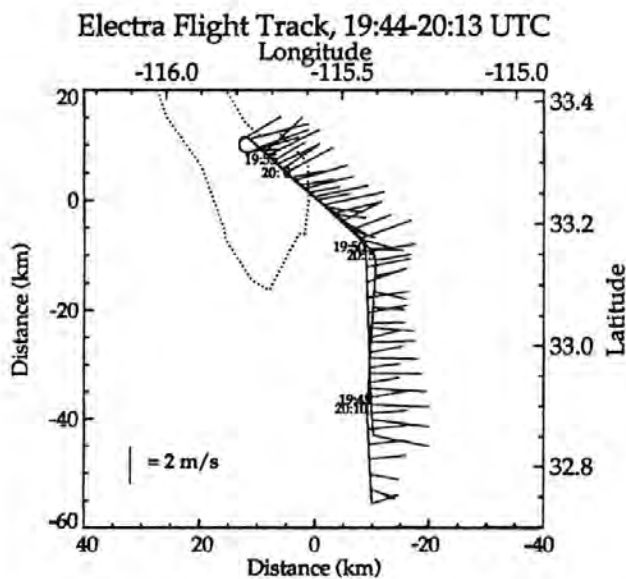


Figure 1 A portion of the Electra flight track on 17 December, 1993. Solid line with time markers represents the track. Dotted line outlines the location of the Salton Sea. Wind lines begin along the flight track and point into the wind. They are proportional in length to the wind speed. Distance is shown relative to the location of the intersection of the flight track with the sea-land boundary. For the times shown the Electra was flying about 1550 m above ground, well above the boundary layer.

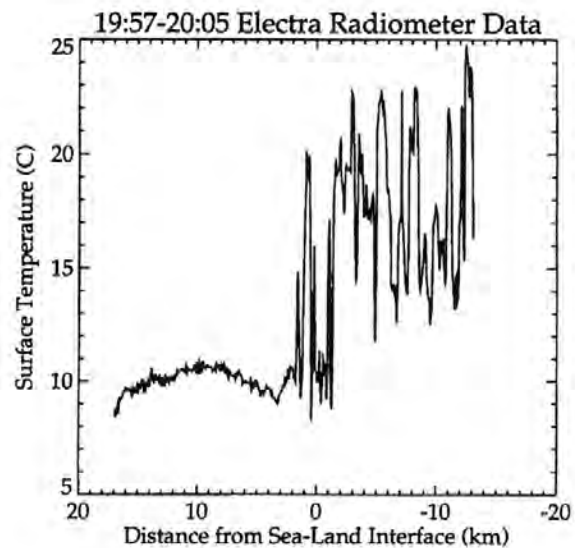


Figure 3 A plot of surface temperature across the sea-land boundary as observed by the downward-looking infrared radiometer on board the NCAR Electra. Note the great variability in land surface temperatures corresponding to different agricultural fields.

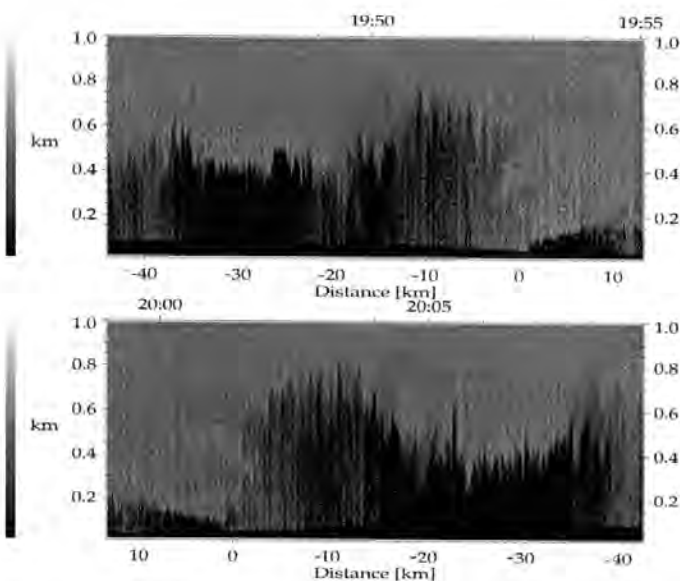


Figure 2 Two dimensional lidar backscatter profiles measured during the time periods 19:45:00–19:55:00 and 19:59:00–20:09:00. The somewhat indistinct land-sea boundary was crossed at about 19:53 and 20:01. The planetary boundary layer can be identified by the increased backscatter due to the high aerosol concentration. Two water vapor absorption lines of different strength were used on the two flight legs.

shown by the dotted outline. This valley is surrounded by dry mountain terrain some distance away to the east and west, and very near around the northern shore of the Salton Sea. The sea and agricultural valley are below sea level.

The Electra and King Air flew wing-to-wing inter-comparisons as well as flight legs on the same track but at different altitudes. Both flew legs at varying altitudes within the boundary layer over the land measuring turbulent fluxes of momentum, heat, water vapor and carbon dioxide. At times the Electra flew above the boundary layer with the DIAL pointing downwards along the flight track shown while the King Air flew below for inter-comparison. The Electra released several dropsondes during its lidar legs. The flight on 17 December included three periods when the Electra overflowed the King Air, with two periods in between when both aircraft flew boundary layer flux legs. The coordinated mission started at 18:15 UTC (10:15 Pacific standard time) and ended at 21:45 UTC.

4 Land and Sea Boundary Layer Structure

Figure 2 shows the lidar backscatter observations collected during the segment of the flight on 17 December shown in Figure 1.

The PBL is clearly identified by the regions of increased lidar backscatter caused by high aerosol

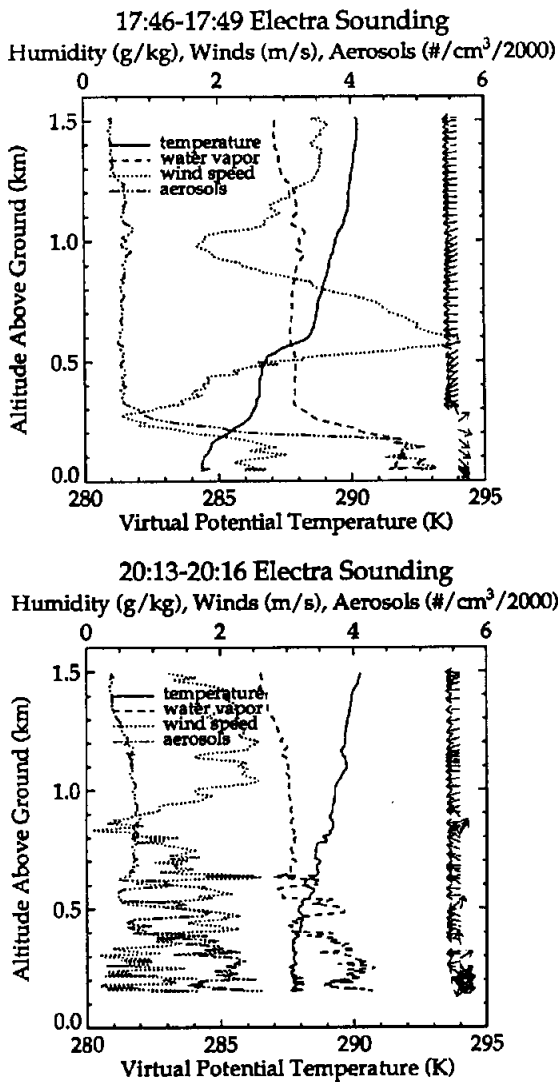


Figure 4 Two in situ soundings over land from the NCAR Electra showing the a) early morning and b) midday convective boundary layer. The arrows on the right point in the direction the wind was blowing, with a downward pointing arrow representing a north wind and an arrow pointing right representing a west wind.

concentrations. The boundary layer over the land was convective and varied greatly in height along the flight track, from about 400 to 600 m, with an elevated area about 800 m deep near the sea-land boundary. This variability was evident in intermittent turbulence observed when flying at upper altitudes within the boundary layer, though the cause of this intermittency is greatly clarified by the lidar image. In situ measurements show approximately 200 W m^{-2} surface fluxes of sensible and latent heat driving convection over the land. The lake boundary layer was very shallow, 100 to 200 m deep. Fluxes were not measured within this layer, but the surface temperature as observed by the downward-looking IR radiometer on board the

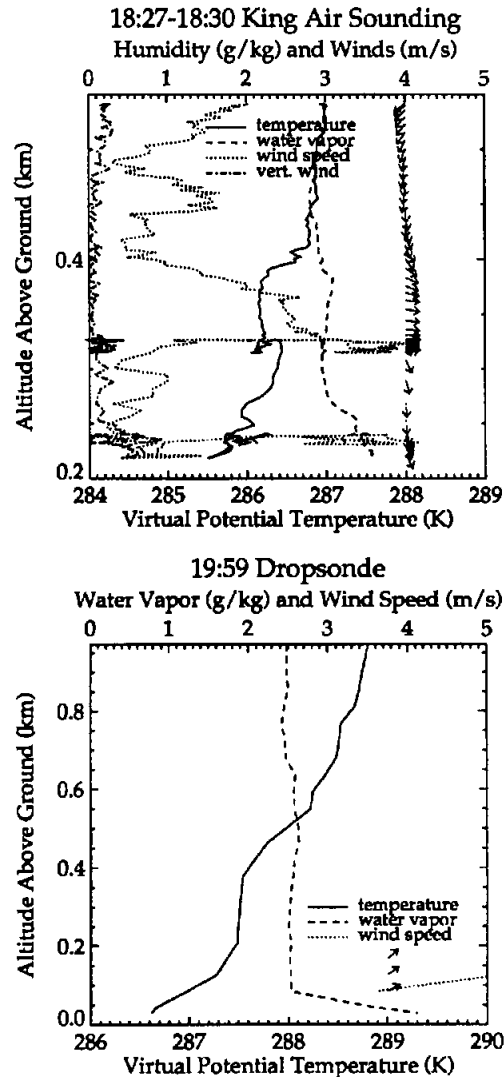


Figure 5 Two soundings over the Salton Sea, one a) from the King Air and one b) from an Electra dropsonde showing persistent stable stratification.

Electra showed the sea surface temperature to be only 9-10 degrees C compared to about 12-25 degrees over the land (see Figure 3). Given the smoothness of the top of the lake PBL as seen in the lidar image, and the cool surface temperatures, we expect this layer to be stably stratified.

The soundings shown in Figure 4 and Figure 5 confirm the structures seen in the lidar images. Figure 4 shows two Electra in situ soundings taken at the southern end of the agricultural region. The first sounding was earlier in the day when the boundary layer was shallow, the inversion was sharp, and a weak, lowlevel jet appeared to flow east to west at the top of the residual boundary layer (the layer that was likely the previous day's convective

boundary layer). The second sounding (4b), taken immediately after the lidar data shown in Figure 2b, shows that the boundary layer had grown to the level of the residual inversion. Prevailing winds were light and from the east above the boundary layer, and very light, perhaps primarily from the west within the boundary layer. The PBL entrainment zone was very highly structured later in the day, as seen in Figure 4b between 400 and 600 m altitude. The Electra aerosol profile in Figure 4b confirms the lidar measurements in Figure 2b, where enhanced aerosol backscatter is observed in the PBL up to an altitude of 650 m at about 20:09.

Two soundings over the Salton Sea, one from an Electra dropsonde and one via the King Air, are plotted in Figure 5. Note that the dropsonde water vapor values were found to be significantly lower than those observed by the Electra in a comparison over the land. Dropsonde wind speeds could be computed only over a limited range due to the relatively low release altitude. Nevertheless, both the sonde and the King Air show a very shallow, stable boundary layer over the sea, as suggested in the lidar images. The same residual convective boundary layer structure as was observed over the land in Figure 4a appears to have been present in both soundings over the sea, despite the lack of convective forcing at the sea surface. The air over the sea up to 500 m altitude did warm somewhat over the course of the day, despite no evidence of heating from below.

5 Water Vapor Intercomparison

We examine the lidar leg flown in Figure 1 to evaluate the water vapor measurements from the DLR DIAL. On the first half of the leg, heading north and northwest, a strong absorption line with a line strength of $S_0 = 27.304 \times 10^{-24} \text{ cm}^{-1} \text{ cm}^2 \text{ mol}^{-1}$ (Grossmann and Browell, 1989a) was selected. Above the lake the DIAL was switched to a weaker line with a line strength of $S_0 = 9.249 \times 10^{-24} \text{ cm}^{-1} \text{ cm}^2 \text{ mol}^{-1}$ (Grossmann and Browell, 1989a), thus enabling us to compare the measurements on a nearly identical flight track heading southeast and south. One can see from Figure 2 that the probed volumes for the two measurements are similar but show some differences which are probably due to the slight deviation of the flight track, shown in Figure 1.

Since the boundary layer structure above the land was so variable, we preferred the flight track above

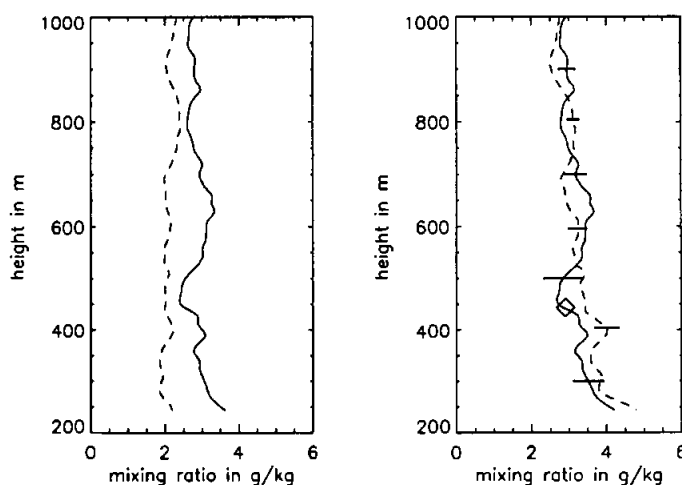


Figure 6 Line intercomparison for the time segments 19:53:00–19:55:00 (strong absorption line, dashed) and 19:59:00–20:01:00 (weaker absorption line, solid) above the sea ($\Delta R = 200 \text{ m}$). Each profile is an average over the given time segments. On the left hand side the uncorrected profiles, on the right the corrected values. The diamond shows the mean mixing ratio measured by the King Air during the same time period.

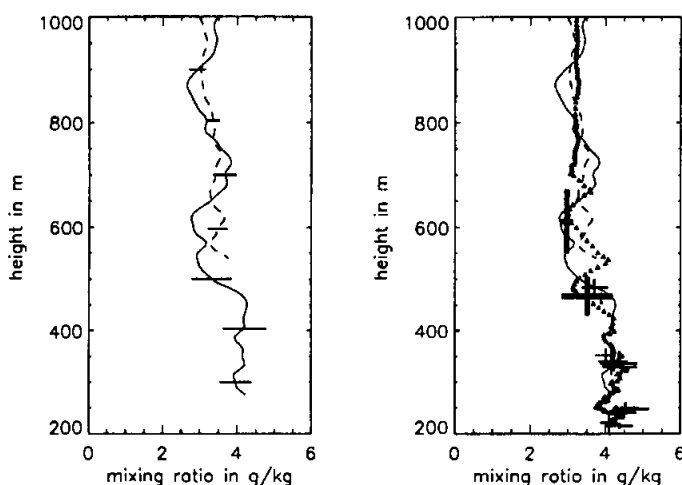


Figure 7 Average water vapor profile for the time segments 20:05:00–20:07:00 (weak absorption line, solid) and 19:47:00–19:49:00 (strong absorption line, dashed) ($\Delta R = 200 \text{ m}$) over the agricultural area. The in situ data are included in the plot on the right. The triangles represent the Electra sounding beginning at 20:14, also shown in Figure 4b. The thick crosses show the King Air EG&G (chilled-mirror) hygrometer in situ values during the lidar leg. The other crosses denote mean in situ values of King Air and Electra chilled-mirror hygrometers observed on constant altitude flight legs collected before (19:04–19:40) and after (20:15–20:53) the lidar leg but along the same flight track. All error bars are standard deviations.

the lake for a line intercomparison. Figure 6 shows the result of the line intercomparison. The left hand plot shows the uncorrected vertical profiles of average water vapor from the two different absorption lines. These profiles represent average values over a horizontal distance of about 11 km and a vertical range cell of 200 m. Both measurements underestimate the water vapor concentration because of the spectral deformation of the on-line laser pulse as it is absorbed by the water vapor. One can also see that because of the higher absorption (better contrast between on- and off-line signals) the measurement on the stronger line is less noisy but it shows a larger systematic error. On the right side of Figure 6 the corrected values demonstrate that the two profiles can be matched. The error bars are standard deviations derived from observations of statistical noise in the on- and off-line signals which were propagated through a simple error propagation calculation for the DIAL equation.

Since the laser line spectral profile is approximated by a simple model of two spectral distributions, one for the central laser peak and one for the broadband emission, the correction scheme becomes inaccurate for large optical depths, where the less-known spectral profile of the broadband radiation begins to play a more dominant role. Furthermore, the signal strength for large optical depths approaches the background radiation causing a large statistical error and high sensitivity to electronic noise. Therefore the corrected profile derived from the strong absorption line is not accurate at low altitudes and was cut off in Figure 7. This means that using the stronger absorption line one can measure accurately over a short range, while the weaker line shows sufficient on-line absorption and better statistics at a more distant range.

The bandwidth of the narrow-band part of the laser line profile was measured during this line intercomparison giving a value of 0.026 cm^{-1} . This value is small in comparison to the spectral width ($\approx 0.16 \text{ cm}^{-1}$) of the molecular lines thus range dependent errors caused by a finite laser line profile can be neglected. From the correction scheme we found that 73.1 % of the total laser radiation emitted into the atmosphere is contained within the narrow-band part of the laser line spectral profile. The residual, unabsorbed background emission is responsible for the difference in water vapor profiles observed when using the strong versus the weak water vapor absorption lines. From a sensitivity analysis we found that the spectral shape of the broadband radiation has no significant

influence on the quality of the line intercomparison. The spectral purity of the dye-laser system is related to a number of specific laser parameters which can change during a long term DIAL measurement. To account for this, the dye laser performance is currently controlled by the PAS cell and Fizeau spectrometer reading which both are monitored in the aircraft cabin. In addition, the pulse energy of the dye-laser is measured for each laser shot. During the pre-BOREAS measurements reported in this study, there was no remarkable change in the quality of the laser spectral purity observed. We finally note that the strong absorption line is only selected because of its sensitivity to the line intercomparison correction procedure. For DIAL measurement in the PBL weaker water vapor absorption lines are preferred.

The in situ value plotted in Figure 6 was measured by the King Air flying below the Electra. This value was measured by the King Air's chilled-mirror hygrometer (EG&G, Waltham, MA, USA), which was shown in wing-to-wing intercomparisons to be consistently about 0.2 g/kg drier than the chilled-mirror hygrometer on the Electra (General Eastern, Watertown, MA, USA), and 0.7 g/kg drier than the infrared absorption hygrometer (LI-COR, Lincoln, NE, USA) on the King Air.

For the in situ intercomparison, a two minute (12 km) leg above the agricultural area where the PBL height was fairly constant was chosen. The left hand plot in Figure 7 shows the average water vapor profiles obtained with the different absorption lines. The PBL top can be seen from the gradient in the water vapor mixing ratio at about 500 m, which agrees well with the aerosol data. On the right hand side one can see the comparison with in situ aircraft data. The Electra sounding shown in that figure was taken 6 minutes after this profile was measured, nearly 35 km to the south. The standard deviation of the difference between the two DIAL profiles in the altitude range of 550–1000 m is 10 % of the mean. Since the PBL height was quite variable, we would expect differences between the Electra sounding and lidar data in the entrainment zone. The thick crosses represent the measurements of the King Air flying below the Electra at the same time the lidar data were being collected. The horizontal and vertical parts of each cross show the standard deviations of the altitudes and mixing ratios averaged along the King Air flight path. The other crosses indicate mean mixing ratios measured on 8–9 min (40–50 km) flight legs above the agricultural area between 19:00 and 21:00 by the Electra and

King Air. As one can see, the values agree well. Between 300 and 1200 m altitude the difference between the Electra sounding and the DIAL water vapor profile (weak line) measured just before the sounding shows a standard deviation of 0.3 g/kg.

6 Sea-Land Interface

Figures 8 and 9 show the two dimensional water vapor and aerosol distributions observed across the sea-land boundary. For the calculation of the water vapor distribution, the data were smoothed over 200 shots (a horizontal distance of about 4.5 km). ΔR was chosen to be 300 m, and the water vapor from this calculation was vertically smoothed over 100 m, which is 13 range bins. The mean relative statistical uncorrelated noise induced error for this figure is 7.5%. A possible systematic error arises from the fact that the on- and off-line shots are not simultaneously, but sequentially emitted from the laser. Thus, different air masses are probed for the on- and off-line measurements. This causes trouble if the backscattering medium is heterogeneous and the backscatter signals are uncorrelated from shot to shot. An autocorrelation analysis applied to horizontal backscatter series measured along the flight leg of Figure 9 however reveals that adjacent backscatter signals are correlated for horizontal separations up to 200 m within the boundary layer and across the boundary layer top. This is more than the distance from one probed atmospheric volume to another, which is 12 m. Aerosol gradients across the land-sea interface are more gentle than those observed at the PBL top over land. The maximum error induced by the offset between on- and off-line shots has been estimated to be 2% for the data presented in Figure 9. This is much smaller than the statistical error of 7.5%.

The measurement used the weak absorption line and the correction scheme has been applied. Aerosol and water vapor show a similar structure across the sea-land transition. A tongue of moist, high aerosol content air 100–200 m deep extends from the land PBL over the sea at about 600 m altitude for a few kilometers. Note that the horizontal extent of this layer is exaggerated in the water vapor plot due to the 4.5 km horizontal smoothing. Another moist, high-aerosol 100–200 m deep layer (the sea PBL) lies just above the sea surface, while a dry, low-aerosol layer lies between these two moist layers. These images superficially resemble a sea-breeze and are remarkably similar to those ob-

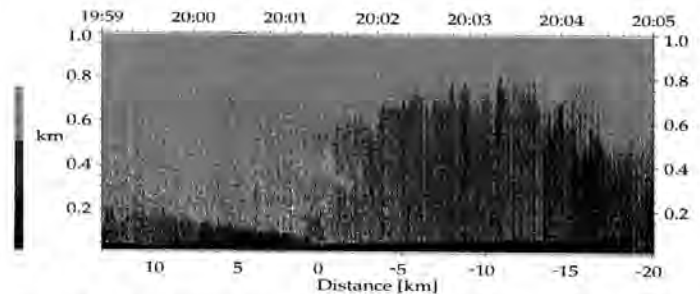


Figure 8 Two dimensional lidar backscatter profiles of the sea-land boundary.

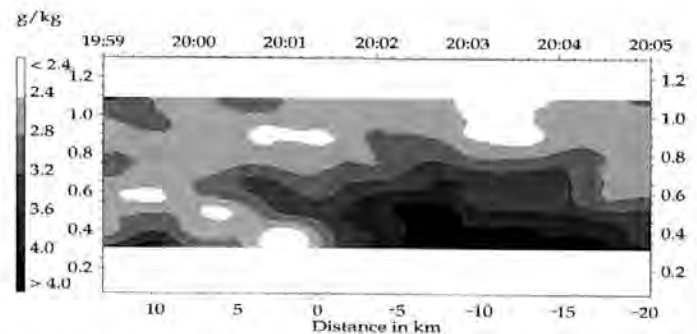


Figure 9 Two dimensional water vapor distribution for the same time segment as Figure 8. The raw data was smoothed over 200 shots. ΔR was chosen to be 300 m. The ordinate values indicate the altitude in km, like in Figure 8.

served by the NASA Langley airborne water vapor DIAL over the Virginia coast (Higdon et al., 1994). They concluded they had observed a sea breeze circulation, though they lacked in situ verification.

In situ observations from the King Air confirm the two dimensional structure observed with the DIAL. Figure 10 shows measurements from level 200 m and 400 m King Air flight legs across the sea-land boundary. These flight tracks are plotted as a function of distance from the shore and altitude in Figure 11a. The water vapor mixing ratios observed by the EG&G chilled-mirror hygrometer and plotted in Figure 10 show the sharp transition from dry to moist conditions which occurs at the sea-land boundary, confirming the transition seen in Figure 9. The vertical velocity measurements 10a also clearly show the change from the turbulent convective boundary layer over land to the stably stratified air over the sea. At about 15 km over the sea, the 200 m level legs shown in Figure 10a begin to penetrate the cold, moist sea PBL seen in the lower left of Figures 8 and 9 as high aerosol backscatter and high mixing ratio, respectively. Figure 11b contains a sketch labelling the different air masses in this region.

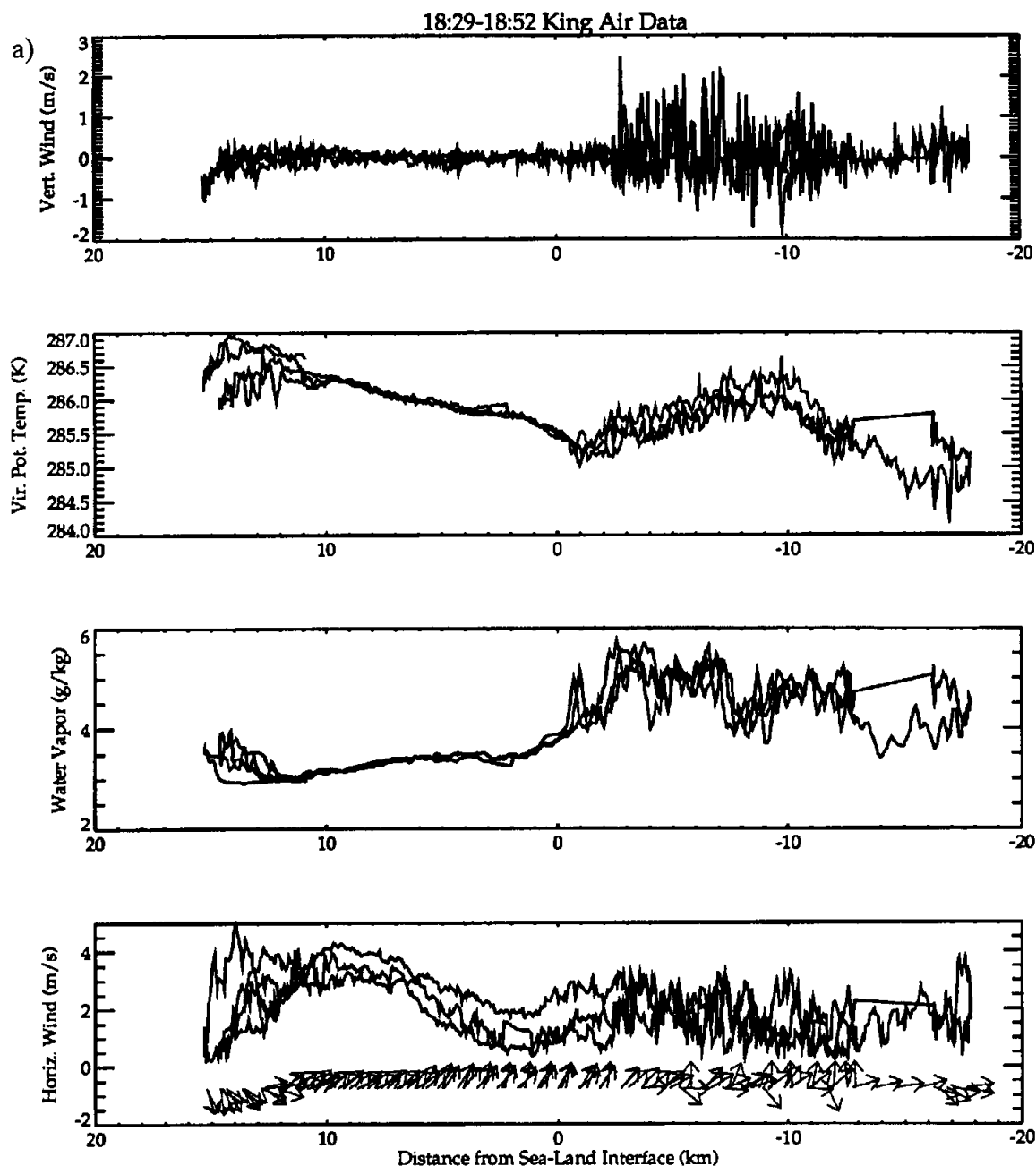


Figure 10a King Air data from level leg run across the sea-land boundary at 200 m and 18:29–18:53 UTC. Arrows point in the direction the wind was blowing.

A slanting descent across the boundary, starting at high altitude over the land and ending at 400 m over the sea, is shown in Figure 12. This flight track is also plotted in Figure 11a. It shows evidence of moist air between 500 and 700 m advecting over dry air at the sea-land interface, as observed in Figure 9. Figure 11a summarizes the water vapor field observed by the King Air, and shows superimposed the PBL top obtained by searching for sharp increases in aerosol backscatter from the lidar data using a wavelet-based edge-detection algorithm. Note the contrast between the moist land PBL and the dry free-troposphere, also clearly seen in Figure 9.

The temperature observations presented in Figure 10 indicate that the 500–700 m flow is not a sea-breeze as might be guessed from Figures 8 and 9, and the surface temperature differences observed in Figure 3. Both flight segments show that the virtual potential temperature steadily increases over the sea with two exceptions: the point at which the sea PBL is intersected (shown in Figure 10a) and a turbulent interface of some sort about 10 km from the shoreline over the sea. While we cannot rule out the possibility of a sea-breeze circulation very near the surface in the shallow sea-PBL, the proper temperature conditions do not seem to exist in the

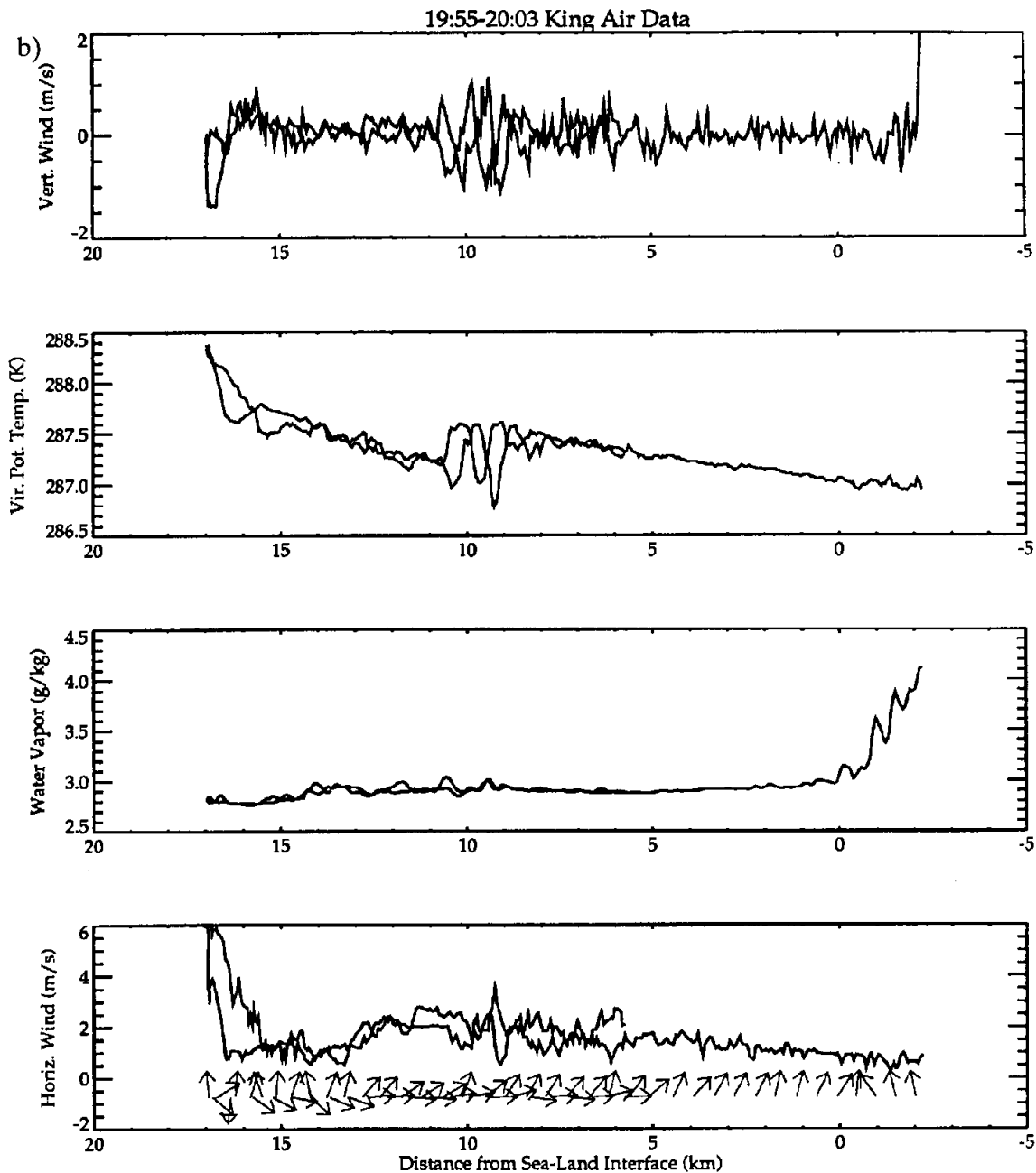


Figure 10b King Air data from level leg runs across the sea-land boundary at 400 m and 19:55–20:03 UTC. Arrows point in the direction the wind was blowing.

dry intermediate layer shown in Figure 9. The winds shown in Figure 10, however, do blow north-north-east, directly towards the nearest shore.

A larger-scale flow pattern explains this onshore wind and the DIAL water vapor field shown in Figure 9 and verified by the in situ data presented in Figures 5, 10, 11a and 12. Figure 13 is a three-dimensional view of the entire King Air flight track shown in two dimensions in Figure 1, and plotted in varying shades of gray corresponding to variations in virtual potential temperature. The winds markers reveal a pattern suggested in the soundings. Above the boundary layer, prevailing easterly winds domi-

nate. These winds are driven by the synoptic conditions at that time, which included a weak high-pressure system to the northeast. Below about 400–500 m, the winds were generally from the west. The same conditions existed over the agricultural region to the south and over the Salton Sea, with two exceptions: The winds over the Salton Sea had more of a northerly component than those in the agricultural boundary layer, and the dry, stable air mass over the sea had a potential temperature more like the air above the agricultural boundary layer than that within the land PBL. The flow below 500 m, fairly uniform throughout the valley, may have been

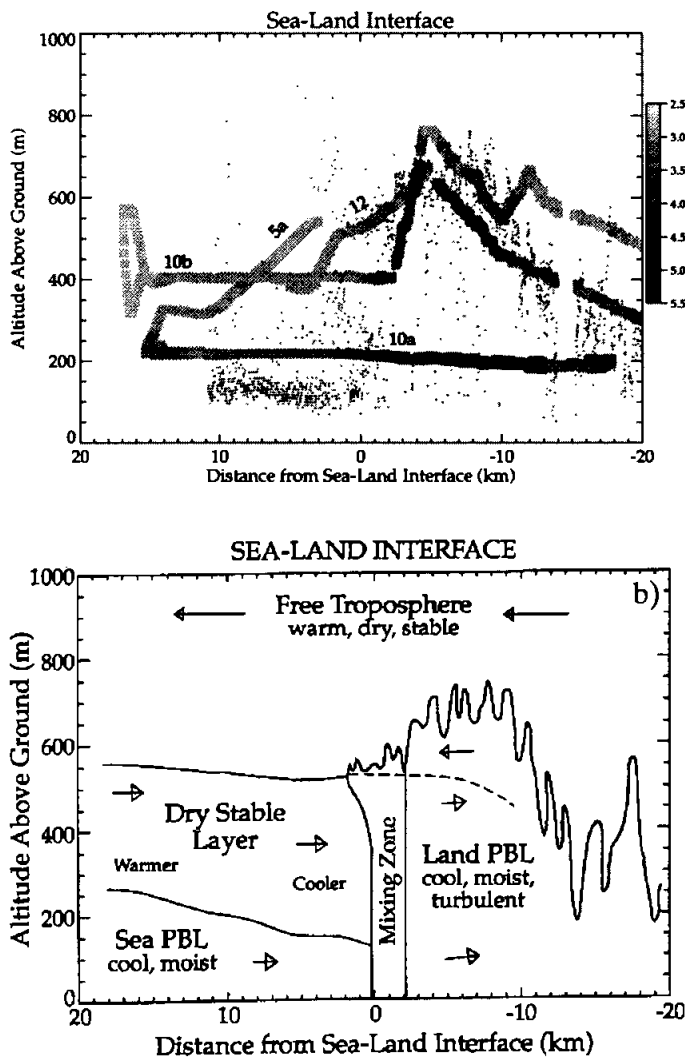


Figure 11 a) Distance vs. height plot of King Air flight legs over the sea-land boundary along the northwest to southeast track shown in Figure 1. Those segments which make up Figures 5a, 10 and 12 are labeled as such. Water vapor values in g/kg are represented by the gray shading of the flight track as described by the key. The dots overlaid on the plot are the locations of sharp changes in aerosol backscatter indicative of boundaries between PBL and free-tropospheric air. b) Schematic of the various air masses at the sea-land boundary, based on the observations summarized in Figure 11a. Arrows show wind direction parallel to the plane of this figure, and length is roughly proportional to wind speed. The dotted line in the center of the figure shows the approximate altitude at which the wind changes direction within the land PBL and the mixing zone. Temperature terms refer to virtual potential temperature.

driven by solar heating of the dry, southwest-facing mountain slopes to the north and east. These mountains rise about 700 m above the Salton Sea and are within 5 to 30 km of much of the flight track. The elevated PBL at the shore may have been caused by frictional convergence.

We conclude that the origin of the moist plume extending over the sea was the vertical wind shear concentrated at about 500 m and shown in Figures 12 and 13. This completes the conceptual picture shown in Figure 11b. The moist, aerosol laden air seen extending over the sea at about 600 m in Figures 8 and 9 advected westward from the entrainment zone of the land PBL and mixed with the more buoyant, drier and cleaner air above the shallow sea PBL which is advected eastwards. In the entrainment zone of a convective PBL, buoyancy increases and turbulence decreases with height. Thus the entrainment zone mixed into the dry layer over the sea from the bottom up, with the top of the entrainment zone maintaining its high aerosol and water vapor content the farthest west, gradually mixing downwards and disappearing as it met with the increasing (about 1 K per 15 km) buoyancy of the dry layer above the sea. Figure 12 captures a slice across the two airmasses. The westward flowing mixture of land PBL and free-tropospheric air which was the land PBL entrainment zone is observed above about 0.5 km. Below this level we see the dry, stable, eastward flowing air mass above the sea.

7 Conclusions

We have tested the DLR DIAL during boundary layer flights over the Imperial Valley of California. It has been shown able to accurately observe very fine scale boundary layer structures in aerosol backscatter, and broader scale features in water vapor. The water vapor mixing values derived from the DIAL observations were within 10 % of in situ values. The DIAL observed what superficially resembled a sea-breeze at the shore of the Salton Sea. In situ observations show density conditions which are not consistent with a sea-breeze scenario. We hypothesize that the observed structure was due to wind shear caused by synoptic flow from land-to-sea above about 500–600 m, and below that level, a sea-to-land flow not caused by the sea-land temperature difference. This hypothesis is consistent with the available in situ and remote observations. This complex meteorological scenario could not have been described without the combination of in situ and remote observations.

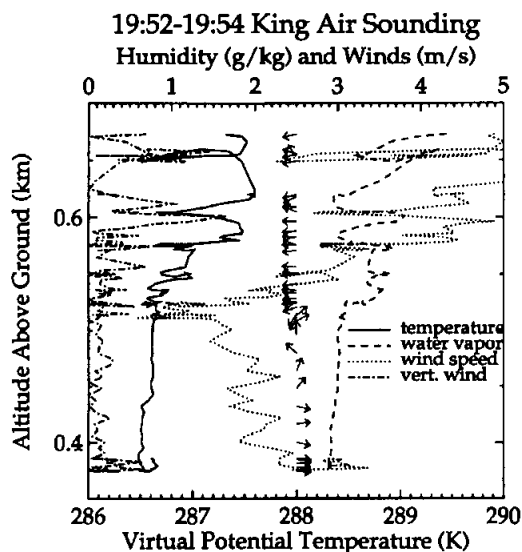


Figure 12 King Air sounding across the sea-land interface, representing data from 19:52–19:54 UTC. Arrows point in the direction the wind was blowing. The magnitudes of vertical velocity fluctuations are plotted on the far left.

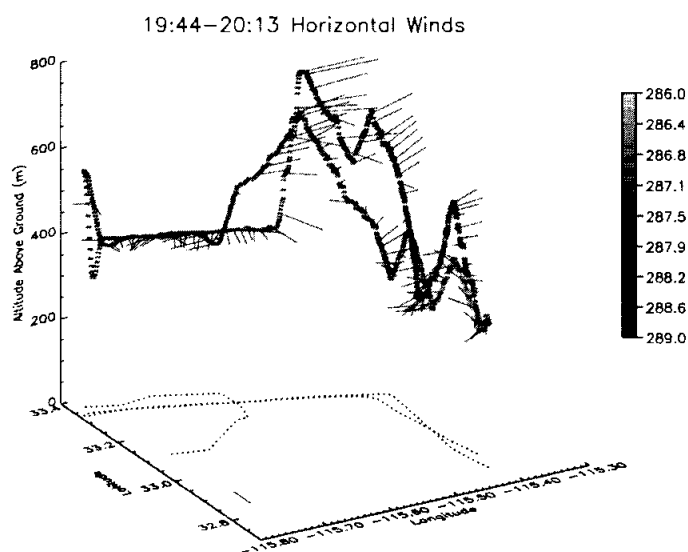


Figure 13 A three-dimensional view of the King Air flight track shown in Figure 1 and shaded gray to correspond with virtual potential temperature in degrees Kelvin. Wind lines begin along the flight track and point into the wind. Their length is proportional to the wind speed. A 2 m s^{-1} wind mark is drawn in the lower left corner of the zero altitude plane for reference. Also drawn on the zero altitude plane are the outline of the Salton Sea and the projection of the King Air flight tracks.

8 Acknowledgements

University of Wyoming participation in this study was supported by National Aeronautics and Space Administration, under grant NAG-5-2240. The King Air facility is supported in part by the National Science Foundation, under a cooperative agreement with the University of Wyoming. Many of the instruments used in this study were new to the King Air. Special thanks are due to the following individuals at U.W. who were involved in the installation and testing: G. Bershinsky, M. Burr, K. Endsley, E. Gasaway, G. Gordon, R. Hansen, L. Irving, C. Kiefer, D. Lukens, A. Rodi, and P. Wechsler. NCAR Electra participation was partly supported by NASA Grant No. S-12857-4. The National Center for Atmospheric Research is supported by the National Science Foundation. The Electra is maintained and operated by NCAR's Research Aviation Facility. The authors acknowledge helpful comments from Andrew Crook and Ron Schwiesow. The Institute for Atmospheric Physics is part of the German Aerospace Research Establishment (Deutsche Forschungsanstalt für Luft- und Raumfahrt (DLR)). The authors would like to thank Norm Zrubeck and Georg Simmet for the technical support during the first installation of the DIAL on the Electra and the DLR for funding a research fellowship.

References

- Browell, E. V., S. Ismail and B. E. Grossmann, 1991: Temperature sensitivity of differential absorption lidar measurements of water vapor in the 720 nm region: *Appl. Opt.* **30**, 1517–1524.
- Ehret, G. and W. Renger, 1990: *Optical Remote Sensing of the Atmosphere*. Optical Society of America, Washington, D.C., 586–589.
- Ehret, G., C. Kiemle, W. Renger and G. Simmet, 1993: Airborne remote sensing of tropospheric water vapor using a near infrared DIAL system: *Appl. Opt.* **32**, 4534–4551.
- Grossman, B. E. and E. V. Browell, 1989a: Spectroscopy of water vapor in the 720 nm region: line strengths, self induced pressure broadenings and shifts, and temperature dependence of linewidths and shifts: *J. Mol. Spectrosc.* **136**, 264–294.
- Grossman, B. E. and E. V. Browell, 1989b: Water vapor line broadening and shifting by air nitrogen, oxygen, and argon in the 720 nm wavelength region: *J. Mol. Spectrosc.* **138**, 562–595.
- Higdon, N. S., E. V. Browell, P. Ponsardin, B. E. Grossmann, C. F. Butler, T. H. Chyba, M. N. Mayo, R. J. Allen, A. W. Heuser, W. B. Grant, S. Ismail, S. D. Mayor and

- A. F. Carter*, 1994: Airborne differential absorption lidar system for measurements of atmospheric water vapor and aerosols: *Appl. Opt.* **33**, 6422–6438.
- Ismail, S.* and *E. V. Browell*, 1989: Airborne and spaceborne lidar measurements of water vapor profiles: a sensitivity analysis: *Appl. Opt.* **28**, 3603–3615.
- Kiemle, C., M. Kaestner* and *G. Ehret*, 1995: The convective boundary layer structure from lidar and radiosonde measurements during the EFEDA'91 campaign: *J. Atmos. and Oceanic Tech.* **12**, 771–782.
- Lenschow, D. H.*, 1986: Probing the Atmospheric Boundary Layer. American Meteorological Society, Boston, MA, 39–55.
- Meischner, P. F., C. Kiemle, G. Ehret, M. Kaestner, H. G. Schreiber, A. V. Evtushenko, B. G. Kutuza, B. Z. Petrenko* and *M. T. Smirnov*, 1994: Remotely sensed water vapor variations during CLEOPATRA '92: *Beitr. Phys. Atmosph.* **67**, 287–301.
- Schootland, R. M.*, 1966: Some observations of the vertical profile of water vapor by means of a laser optical radar, 1966: Proceedings of the Fourth Symposium on Remote Sensing of Environment. University of Michigan, Ann Arbor, Mich., 273–277.
- Schootland, R. M.*, 1974: Errors in the lidar measurement of atmospheric gases by differential absorption: *J. Appl. Meteorol.* **13**, 315–331.